

3-D EM Scattering and Inverse Scattering by Anisotropic Objects Straddling Multiple Planar Uniaxial Layers With a 2-D Locally Rough Surface

Ruidong Huang, Qing Wu, and Feng Han¹, *Senior Member, IEEE*

Abstract—In this article, both the electromagnetic (EM) forward and inverse scattering by 3-D arbitrary anisotropic scatterers straddling multiple planar uniaxial layers covered by a 2-D locally rough surface are discussed. In the forward scattering, the 3-D electric field integral equation (EFIE) is formulated and the dyadic Green's functions (DGFs) are evaluated based on the transmission-line analogy method and the buried object approach (BOA) to account for the EM wave reflection in multiple planar layer boundaries and its scattering from the rough surface. The additional computational cost caused by the rough surface is theoretically analyzed. In the full-wave inversion (FWI), the discretized data equation which is assembled from the total fields solved from the forward EFIE and the DGFs including the rough surface influence is solved by the variational Born iterative method (VBIM). Several numerical examples are presented to verify the computation accuracy and the additional time and memory cost caused by the rough surface in the forward scattering and to testify to the necessity to include the rough surface in inverse scattering.

Index Terms—3-D inverse scattering, anisotropy, buried object approach (BOA), multilayered media, rough surface.

I. INTRODUCTION

ELECTROMAGNETIC (EM) scattering and inverse scattering are important research branches in the EM community. They have many applications such as near-surface detection [1], microwave imaging [2], geophysical prospecting [3], and high-speed circuit design [4].

One of the most important methods to solve EM scattering and inverse scattering problems is using integral equations. In the forward scattering, the integral equation is discretized and the obtained algebraic equation is originally solved by the method of moments (MoM) [5]. Unfortunately, direct matrix inverse in the MoM usually has an unaffordable computation cost [6]. Several fast algorithms have been proposed to lower both the computation time and memory consumption. It is usually achieved by the iterative implementation of matrix-vector multiplication which is often accelerated by

fast Fourier transform (FFT) or by the decomposition of near-field and far-field interactions between equivalent current and Green's functions. For example, the conjugate gradient FFT (CG-FFT) [7] is a typical iterative method that transforms the spatial-domain convolution of the equivalent current and Green's functions inside the computational domain into spectral-domain algebraic multiplication. Based on this core idea, researchers have proposed several improved methods such as biconjugate gradient-FFT (BCG-FFT) [8] and the stabilized BCG-FFT (BCGS-FFT) [6]. Compared with MoM, these improved FFT-based methods are able to lower the computation time from $O(N^3)$ to $O(KN\log N)$ where K is the iteration number and memory consumption from $O(N^2)$ to $O(N)$. The fast multipole algorithm (FMA) is different from the FFT-based methods. Its implementation is based on the decomposition of the computational domain and the addition theorem [9]. FMA was later further developed into the multilevel FMA (MLFMA) [10], [11] in which the domain decomposition and addition theorem are implemented at different levels. In the adaptive integral method (AIM) [12], the MoM matrix is decomposed into a sparse near-field part and a dense far-field part whose multiplication with a vector fortunately can be accelerated by FFT.

In EM inverse scattering, due to the intrinsic nonlinearity and ill-posedness, the model parameters of the scatterers are always obtained by iteratively minimizing the least-square cost function with a penalty term. In this process, the aforementioned forward scattering methods are usually called several times. The popular full-wave inversion (FWI) methods mainly include Born-type methods, contrast source inversion (CSI), subspace-based optimization method (SOM), and their hybridization. In the Born-type methods, the nonlinear EM scattering data equation is linearized by replacing the total fields inside the computational domain in the current iteration with those computed in the last iteration. The major difference among these Born-type methods is that the Born iterative method (BIM) [13] directly updates the model parameters while the variational BIM (VBIM) [14] updates their variations in each iteration. In the distorted BIM (DBIM) [15], Green's functions of the background medium are also updated in each iteration. CSI is different from Born-type methods since its cost function includes not only the mismatch in the data equation but also the mismatch in the state equation [16], [17]. The contrast and the contrast source are alternatively updated

Manuscript received 30 April 2023; revised 21 July 2023; accepted 23 August 2023. This work was supported by the National Natural Science Foundation of China under Grant 62271428. (Corresponding author: Feng Han.)

The authors are with the Institute of Electromagnetics and Acoustics and the Key Laboratory of Electromagnetic Wave Science and Detection Technology, Xiamen University, Xiamen 361005, China (e-mail: feng.han@xmu.edu.cn).

Color versions of one or more figures in this article are available at <https://doi.org/10.1109/TAP.2023.3309094>.

Digital Object Identifier 10.1109/TAP.2023.3309094

until the total error is minimized. SOM is similar to CSI. However, the minimization is carried out in a subspace of the induced current [18], [19]. In addition, there are also some hybrid methods combining two of these inversion approaches. For example, in [20], the DBIM and SOM are combined to reach a faster convergence speed than the pure DBIM. One should note that although the aforementioned forward methods have been applied to the computation of EM scattering by 3-D objects with large electrical sizes [21], [22], [23], by 3-D objects with dielectric anisotropy [24], [25], [26], [27], [28], [29], and by 2-D or 3-D objects buried in layered media [26], [27], [28], [29], [30] and the inverse methods have been applied to the reconstruction of 2-D or 3-D objects [30], [31], 2-D or 3-D objects buried in layered media [28], [29], [32], [33], and anisotropic objects [28], [29], [34], [35], the background medium is merely homogeneous or planarly layered and the scatterers are restricted inside one single planar layer in most situations. However, in practical applications of EM inversion, e.g., mine detection [36] and subsurface sensing by ground-penetrating radar [37], the scenario in which the background medium is planarly multilayered but with a locally rough surface and the scatterers are placed across several subsurface planar layers is almost inevitable.

The major influence of the rough surface is the computation of 3-D dyadic Green's functions (DGFs). For a purely planarly multilayered medium, 3-D DGFs are evaluated by the Sommerfeld integration [38]. When the locally rough surface is present, one of the commonly used numerical methods to account for its EM scattering effect is using the buried object approach (BOA) [39]. Its basic idea is that the 2-D rough surface is decomposed into several independent 3-D objects which are treated as scatterers embedded inside the top planar layer and the second one. Then the integral equation involving the DGFs in purely planar layers is adopted to compute the scattering fields generated by the rough surface, which are later added to the layered medium DGFs calculated by the Sommerfeld integration to form the final DGFs of the background medium with a rough surface. Compared with other methods such as the Kirchhoff approximation [40] and the small perturbation method [41], BOA can adapt to rough surfaces of any scale. Therefore, the studies of both forward and inverse scattering by subsurface 3-D objects beneath locally rough surfaces have been accomplished based on the BOA [42], [43]. However, most of these previous works only deal with the half-space model or a limited number of planar layers beneath the rough surface. The subsurface 3-D objects are only placed inside one single planar layer. Meanwhile, the anisotropy of either the background medium or the 3-D scatterers has never been considered.

Therefore, in this article, we deal with the EM forward scattering from and FWI of anisotropic objects straddling multiple subsurface planar uniaxial layers covered by a 2-D locally rough surface. Compared with previous works regarding 3-D EM scattering and inverse scattering based on the BOA [42], [43], our work has the following new contributions. 1) There are several planar layers beneath the rough surface while only the half-space model is considered in previous works. Therefore, the 3-D BOA must be correctly combined

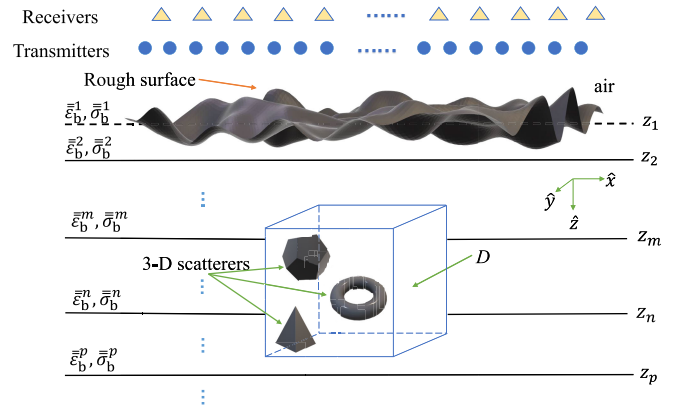


Fig. 1. Configuration of the EM scattering and inverse scattering model for an arbitrary anisotropic 3-D objects buried in a multilayered uniaxial medium with a locally rough surface. Either the 3-D objects or the computational domain D are allowed to straddle multiple planar layers.

with multilayered DGFs. 2) Both the layered background medium and the 3-D scatterers are anisotropic. Meanwhile, the 3-D scatterer with arbitrary anisotropy straddles multiple planar layers with a 2-D rough surface. Such an EM scattering scenario will make the implementation of BOA more difficult than that only for an isotropic half-space model. 3) Totally, 12 anisotropic parameters of the 3-D scatterers beneath a rough surface are simultaneously reconstructed by VBIM. 4) The computational cost and inversion accuracy for the scenarios with and without the rough surface are compared in detail.

The rest of this article is organized as follows. In Section II, a detailed description of the theory is presented. In the forward model, the mathematical formulation of the electric field integration equation (EFIE) for 3-D anisotropic objects straddling planarly multilayered uniaxial medium with a rough surface is given. Then the BOA is used to determine the DGFs of the background medium. The additional computational cost caused by the rough surface is theoretically analyzed. The inversion by VBIM is simply mentioned. In Section III, we verify the forward computation results by comparing them with the numerical simulations of the finite element method (FEM) by the commercial software COMSOL. The computational cost for the EM scattering scenarios with and without the rough surface is quantitatively compared. The related reasons are analyzed. In Section IV, several numerical inversion experiments based on VBIM are carried out to confirm the necessity in consideration of the rough surface. Finally, in Section V, conclusions are drawn and discussions are presented.

II. METHODS

The objective of this work is to solve the EM scattering and inverse scattering problems of the 3-D anisotropic objects placed across multiple planar uniaxial layers which are covered by a 2-D locally rough surface. Meanwhile, the computational cost for the scattering scenarios with and without the rough surface is compared. The typical configuration is shown in Fig. 1. The principal axis of the layered background medium is in the \hat{z} -direction and its permeability is the same as that

of the free space. The relative permittivity and conductivity tensors of the m th layer are written as

$$\bar{\epsilon}_b^m = \text{diag}\{\epsilon_{11}^m, \epsilon_{22}^m, \epsilon_{33}^m\}, \quad \bar{\sigma}_b^m = \text{diag}\{\sigma_{11}^m, \sigma_{22}^m, \sigma_{33}^m\} \quad (1)$$

where $\epsilon_{11}^m = \epsilon_{22}^m$, $\sigma_{11}^m = \sigma_{22}^m$, and the subscript b means the background. The relative complex permittivity tensor of the m th layer is written as

$$\bar{\epsilon}_b^m = \bar{\epsilon}_b^m + \frac{\bar{\sigma}_b^m}{j\omega\epsilon_0} \quad (2)$$

where ω is the angular frequency of the EM wave. The relative permittivity and conductivity tensors of the inhomogeneous scatterer are written as

$$\bar{\epsilon}_s = \begin{bmatrix} \epsilon_{11}^s & \epsilon_{12}^s & \epsilon_{13}^s \\ \epsilon_{21}^s & \epsilon_{22}^s & \epsilon_{23}^s \\ \epsilon_{31}^s & \epsilon_{32}^s & \epsilon_{33}^s \end{bmatrix}, \quad \bar{\sigma}_s = \begin{bmatrix} \sigma_{11}^s & \sigma_{12}^s & \sigma_{13}^s \\ \sigma_{21}^s & \sigma_{22}^s & \sigma_{23}^s \\ \sigma_{31}^s & \sigma_{32}^s & \sigma_{33}^s \end{bmatrix} \quad (3)$$

where $\epsilon_{pq}^s = \epsilon_{qp}^s$ and $\sigma_{pq}^s = \sigma_{qp}^s$ with $p, q = 1, 2$, and 3 . This symmetry is ubiquitous in nature [44]. The relative complex tensor permittivity of the scatterer is written as

$$\bar{\epsilon}_s = \bar{\epsilon}_s + \frac{\bar{\sigma}_s}{j\omega\epsilon_0}. \quad (4)$$

A. 2-D Rough Surface Model

In this work, the 2-D rough surface having the horizontal size $L_x \times L_y$ is generated from the Gaussian spectrum [45]

$$W(K_x, K_y) = \frac{l_x l_y h^2}{4\pi} \exp\left[-\frac{l_x^2 K_x^2 + l_y^2 K_y^2}{4}\right] \quad (5)$$

where $K_x = 2\pi x/L_x$ and $K_y = 2\pi y/L_y$ are the spatial frequencies in the \hat{x} - and \hat{y} -directions, respectively. l_x and l_y are the correlation lengths in \hat{x} - and \hat{y} -directions, respectively. The parameter h represents the root mean square (rms) height of the rough surface. Note we let $l_x = l_y$ in the whole work since only the isotropic rough surface is considered.

B. EM Forward Scattering Model

As shown in Fig. 1, for the 3-D scatterer straddling multiple planar layers and the transceivers placed in the first layer above the rough surface, the EM forward scattering is formulated in the framework of EFIE and expressed via the state equation by

$$\mathbf{E}_{\text{inc}}(\mathbf{r}) = \mathbf{E}_{\text{tot}}(\mathbf{r}) - j\omega\epsilon_0 \int_D \bar{\mathbf{G}}_{\mathbf{EJ}}^{\text{ii}}(\mathbf{r}, \mathbf{r}') \cdot \bar{\epsilon}_b(\mathbf{r}') \bar{\chi}(\mathbf{r}') \mathbf{E}_{\text{tot}}(\mathbf{r}') d\mathbf{r}' \quad (6)$$

where \mathbf{E}_{inc} is the incident electric field evaluated inside the computational domain D when the 3-D scatterer is absent while \mathbf{E}_{tot} is the total electric field when the scatterer is present. $\bar{\epsilon}_b$ is the complex relative permittivity of the background medium inside D which, however, can take different values when \mathbf{r}' locates in different layers. The superscript ii of $\bar{\mathbf{G}}_{\mathbf{EJ}}^{\text{ii}}(\mathbf{r}, \mathbf{r}')$ means both the source point \mathbf{r}' and the field point \mathbf{r} of the DGF locate in the inversion domain D . The contrast function χ is defined as

$$\bar{\chi}(\mathbf{r}) = [\bar{\epsilon}(\mathbf{r}) - \bar{\epsilon}_b(\mathbf{r})][\bar{\epsilon}_b(\mathbf{r})]^{-1} \quad (7)$$

where $\bar{\epsilon}$ is the complex relative permittivity of the inhomogeneous 3-D scatterer. Before we discretize (6) and solve for \mathbf{E}_{tot} using BCGS [26] from it, \mathbf{E}_{inc} is first obtained through

$$\mathbf{E}_{\text{inc}}(\mathbf{r}) = \int \bar{\mathbf{G}}_{\mathbf{EJ}}^{\text{it}}(\mathbf{r}, \mathbf{r}') \cdot \mathbf{J}(\mathbf{r}') d\mathbf{r}' \quad (8)$$

where the superscript it of the DGF $\bar{\mathbf{G}}_{\mathbf{EJ}}^{\text{it}}$ means the source point \mathbf{r}' locates in the transmitter domain in the first layer and the field point \mathbf{r} locates in the inversion domain D . Once \mathbf{E}_{tot} is obtained from (6), the scattered fields \mathbf{E}_{sct} and \mathbf{H}_{sct} are solved by the data equations which are expressed as

$$\mathbf{E}_{\text{sct}}(\mathbf{r}) = j\omega\epsilon_0 \int_D \bar{\mathbf{G}}_{\mathbf{EJ}}^{\text{ri}}(\mathbf{r}, \mathbf{r}') \cdot \bar{\epsilon}_b(\mathbf{r}') \bar{\chi}(\mathbf{r}') \mathbf{E}_{\text{tot}}(\mathbf{r}') d\mathbf{r}' \quad (9a)$$

$$\mathbf{H}_{\text{sct}}(\mathbf{r}) = j\omega\epsilon_0 \int_D \bar{\mathbf{G}}_{\mathbf{HJ}}^{\text{ri}}(\mathbf{r}, \mathbf{r}') \cdot \bar{\epsilon}_b(\mathbf{r}') \bar{\chi}(\mathbf{r}') \mathbf{E}_{\text{tot}}(\mathbf{r}') d\mathbf{r}' \quad (9b)$$

where the superscript ri of the DGFs $\bar{\mathbf{G}}_{\mathbf{EJ}}^{\text{ri}}$ and $\bar{\mathbf{G}}_{\mathbf{HJ}}^{\text{ri}}$ means the source point \mathbf{r}' locates in the inversion domain D and the field point \mathbf{r} locates in the receiver domain in the first layer.

C. Computation of $\bar{\mathbf{G}}_{\mathbf{EJ}}^{\text{it}}$, $\bar{\mathbf{G}}_{\mathbf{EJ}}^{\text{ii}}$, $\bar{\mathbf{G}}_{\mathbf{EJ}}^{\text{ri}}$, and $\bar{\mathbf{G}}_{\mathbf{HJ}}^{\text{ri}}$

In the aforementioned formulas (6)-(9), four types of DGFs including $\bar{\mathbf{G}}_{\mathbf{EJ}}^{\text{it}}$, $\bar{\mathbf{G}}_{\mathbf{EJ}}^{\text{ii}}$, $\bar{\mathbf{G}}_{\mathbf{EJ}}^{\text{ri}}$, and $\bar{\mathbf{G}}_{\mathbf{HJ}}^{\text{ri}}$ are used. We first discuss the EM scattering scenario in which the first layer boundary is flat and the background medium is purely planarly layered. In this situation, the four DGFs can be evaluated using the transmission-line analogy method. Briefly speaking, the spherical wave excited by the 3-D dipole is first decomposed into a series of plane waves in the spectral domain. The transmission and reflection in different layer boundaries of each plane wave component are then computed. Finally, the summation of all the plane waves at the receiver point is performed to obtain the DGFs. The specific spectral expressions are listed in Appendix. For more detailed discussions, readers can refer to [38]. Now, we assume there are totally N_t transmitters and N_r receivers. The inversion domain D is discretized into $N = N_x \times N_y \times N_z$ voxels. For $\bar{\mathbf{G}}_{\mathbf{EJ}}^{\text{it}}$, $\bar{\mathbf{G}}_{\mathbf{EJ}}^{\text{ri}}$, and $\bar{\mathbf{G}}_{\mathbf{HJ}}^{\text{ri}}$, we need to compute $N_t \times N$, $N_r \times N$, and $N_r \times N$ DGFs, respectively. Of course, each DGF tensor actually includes nine components. Special attention should be paid to the computation of $\bar{\mathbf{G}}_{\mathbf{EJ}}^{\text{ii}}$. Since the inversion domain D straddles multiple planar layers, $\bar{\mathbf{G}}_{\mathbf{EJ}}^{\text{ii}}$ no longer can be decomposed into “plus” and “minus” parts in the vertical \hat{z} -direction [26]. However, in light of its spatial shift invariance in the horizontal xy plane, we can still reduce the computational cost for the evaluation of $\bar{\mathbf{G}}_{\mathbf{EJ}}^{\text{ii}}$ and the integration in (6). It is rewritten as

$$\bar{\mathbf{G}}_{\mathbf{EJ}}^{\text{ii}}(\mathbf{r}, \mathbf{r}') = \bar{\mathbf{G}}_{\mathbf{EJ}}^{\text{ii}}(x - x', y - y', z, z'). \quad (10)$$

As a result, we only need to compute $N_z^2 N_x N_y$ instead of N^2 DGFs for $\bar{\mathbf{G}}_{\mathbf{EJ}}^{\text{ii}}$. On the other hand, the integration in (6) is actually a 2-D convolution in the xy plane plus an arithmetic accumulation in the \hat{z} -direction. Therefore, the 2-D FFT can be used to accelerate the convolution. The computation time is lowered from $O(N^3)$ to $O(N_z^3 N_x N_y \log(N_x N_y))$.

Now, let us discuss the computation of the aforementioned four DGFs when the 2-D locally rough surface is present. In this situation, the transmission-line analogy method presented in [38] is no longer valid due to EM scattering caused by the rough surface. Simultaneously, the spatial shift invariance in the xy plane for $\overline{\overline{\mathbf{G}}}_{\text{EJ}}^i$ becomes invalid and we need to compute N^2 DGFs. Meanwhile, the EFIE in (6) can only be solved by the original MoM and the computation time is $O(N^3)$. To account for the rough surface scattering, we adopt the BOA in which the 2-D rough surface shown in Fig. 1 is treated as the combination of a series of 3-D scatterers which are embedded on both sides of the $z = z_1$ plane and these scatterers are defined as BOA objects. The integral equation is then formed and the DGFs are obtained. Although the BOA has been adopted in previous works [39], [42], [43], they are only for half-space models. We will apply the BOA to multiple uniaxial layers in this work. As shown in Fig. 1, the dielectric parameters of BOA objects embedded in different planar layers are different. The relative permittivity and conductivity of those lie in the $z < z_1$ half-space and those lying in the region between the interfaces of $z = z_1$ and $z = z_2$ are $\overline{\overline{\epsilon}}_b^2, \overline{\overline{\sigma}}_b^2$, and $\overline{\overline{\epsilon}}_b^1, \overline{\overline{\sigma}}_b^1$, respectively. Thus, an integral equation method can be adopted to solve for the total DGFs which include both the transmission and reflection in the horizontal boundary and the scattering from those fictitious 3-D objects embedded in the first layer and the second layer. Here, we follow this procedure to derive the total DGFs for 3-D multiple planar layers with a 2-D locally rough surface. We take $\overline{\overline{\mathbf{G}}}_{\text{EJ}}^i$ as the example. The other three DGFs can be derived in the same procedure. For convenience, the subscript of $\overline{\overline{\mathbf{G}}}_{\text{EJ}}^i$ is dropped.

The DGF $\overline{\overline{\mathbf{G}}}^i(\mathbf{r}, \mathbf{r}')$ can be expressed as the summation of two components

$$\overline{\overline{\mathbf{G}}}^i(\mathbf{r}, \mathbf{r}') = \overline{\overline{\mathbf{G}}}_0^i(\mathbf{r}, \mathbf{r}') + \overline{\overline{\mathbf{G}}}_s^i(\mathbf{r}, \mathbf{r}') \quad (11)$$

where $\overline{\overline{\mathbf{G}}}_0^i(\mathbf{r}, \mathbf{r}')$ is the DGF contributed by the 3-D planarly multilayered medium, and $\overline{\overline{\mathbf{G}}}_s^i(\mathbf{r}, \mathbf{r}')$ is contributed by the scattered EM fields generated by the 2-D rough surface. The details of $\overline{\overline{\mathbf{G}}}_0^i(\mathbf{r}, \mathbf{r}')$ can be found in Appendix. To solve for $\overline{\overline{\mathbf{G}}}_s^i(\mathbf{r}, \mathbf{r}')$, we first formulate the state equation to describe the EM scattering by the equivalent 3-D objects of the 2-D rough surface embedded in the planarly multilayered medium. It is written as

$$\begin{aligned} \overline{\overline{\mathbf{G}}}_0^{bo,i}(\mathbf{r}'', \mathbf{r}') &= \overline{\overline{\mathbf{G}}}_t^{bo}(\mathbf{r}'') - j\omega\epsilon_0 \int_{RS} \overline{\overline{\mathbf{G}}}_0^{bo,bo}(\mathbf{r}'', \mathbf{r}'') \\ &\quad \times [\overline{\overline{\chi}}^{bo}(\mathbf{r}'') \overline{\overline{\mathbf{G}}}_t^{bo}(\mathbf{r}'')] d\mathbf{r}'' \end{aligned} \quad (12)$$

where $\overline{\overline{\mathbf{G}}}_0^{bo,i}$ represents the incident field inside the fictitious 3-D buried object regions when the 2-D rough surface is absent. The source point \mathbf{r}' locates inside the inversion domain D while the field point \mathbf{r}'' locates inside the buried objects of the rough surface, as shown in Fig. 1. $\overline{\overline{\mathbf{G}}}_t^{bo}$ represents the total field inside the 3-D buried object regions when the

2-D rough surface is present. $\overline{\overline{\mathbf{G}}}_0^{bo,bo}$ is the DGF in the planarly multilayered medium when both the source point and the field point are inside the buried object regions. The subscript RS denotes the rough surface. $\overline{\overline{\chi}}^{bo}$ represents the dielectric contrast of the 3-D buried objects of the 2-D rough surface with respect to the planarly multilayered background medium and is defined as

$$\overline{\overline{\chi}}(\mathbf{r}'') = \begin{cases} \overline{\overline{\epsilon}}_b^2 - \overline{\overline{\epsilon}}_b^1, & \mathbf{r}'' \in \text{layer 1} \\ \overline{\overline{\epsilon}}_b^1 - \overline{\overline{\epsilon}}_b^2, & \mathbf{r}'' \in \text{layer 2.} \end{cases} \quad (13)$$

Now, we discretize the fictitious 3-D buried objects of the 2-D rough surface into N_b cubic voxels and set \mathbf{r}'' at the center of each voxel. If its volume is small enough, (12) can be discretized and represented in a matrix form

$$\mathbf{K}\mathbf{G} = \mathbf{G}_0 \quad (14)$$

where

$$\mathbf{K} = \left[\mathbf{I} - j\omega\epsilon_0 \overline{\overline{\mathbf{G}}}_0^{bo,bo}(\mathbf{r}_m'', \mathbf{r}_n'') \overline{\overline{\chi}}^{bo}(\mathbf{r}_n'') \right] \Delta V_b \in \mathbb{C}^{(3N_b, 3N_b)} \quad (15a)$$

$$\mathbf{G} = \left[\overline{\overline{\mathbf{G}}}_t^{bo}(\mathbf{r}_n'') \right] \in \mathbb{C}^{(3N_b, 3)} \quad (15b)$$

$$\mathbf{G}_0 = \left[\overline{\overline{\mathbf{G}}}_0^{bo,i}(\mathbf{r}_m'', \mathbf{r}') \right] \in \mathbb{C}^{(3N_b, 3)} \quad (15c)$$

in which ΔV_b is the volume of the discretized cubic voxel, and $m, n \in [1, N_b]$ are the indexes of the voxels. For the matrices \mathbf{K} , \mathbf{G} , and \mathbf{G}_0 , different components of a DGF are arranged in different blocks. Let us take the first column of \mathbf{G} as an example. It is composed of three blocks which are corresponding to the $\hat{x}\hat{x}$, $\hat{y}\hat{x}$, and $\hat{z}\hat{x}$ components of $\overline{\overline{\mathbf{G}}}_t^{bo}(\mathbf{r}_n'')$. Each block has the dimensions of $N_b \times 1$ for which n increases from 1 to N_b . We can solve for the discretized $\overline{\overline{\mathbf{G}}}_t^{bo}$ from (14) using BCGS. Then the discretized $\overline{\overline{\mathbf{G}}}_s^i(\mathbf{r}, \mathbf{r}')$ can be obtained using the following data equation:

$$\overline{\overline{\mathbf{G}}}_s^i(\mathbf{r}, \mathbf{r}') = \sum_{n=1}^{N_b} j\omega\epsilon_0 \overline{\overline{\mathbf{G}}}_0^{r,bo}(\mathbf{r}, \mathbf{r}_n'') [\overline{\overline{\chi}}^{bo}(\mathbf{r}_n'') \overline{\overline{\mathbf{G}}}_t^{bo}(\mathbf{r}_n'')] \Delta V_b \quad (16)$$

where $\overline{\overline{\mathbf{G}}}_0^{r,bo}$ is the planarly multilayered DGF when the source point \mathbf{r}'' is inside the 3-D buried objects of the 2-D rough surface, and the field point \mathbf{r} is at the receiver position. Finally, $\overline{\overline{\mathbf{G}}}^i$ in (11) is obtained to account for the 3-D uniaxial layered background medium with a 2-D rough surface. From the above derivations and discussions, we can see that the computation of DGFs when the rough surface is present is much more time-consuming compared with the situation when the rough surface is replaced with a planar one. This will be verified in Section III. Another important issue is the singularity of $\overline{\overline{\mathbf{G}}}_0^{bo,bo}$ in (15a) when $\mathbf{r}_m'' = \mathbf{r}_n''$. This is discussed in Appendix.

D. EM FWI Model

In the inversion, the complex contrast function $\overline{\overline{\chi}}(\mathbf{r}')$ distribution inside the computational domain D shown in Fig. 1 is

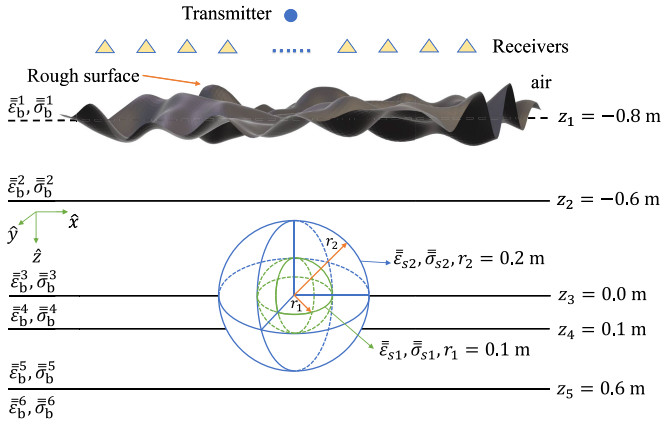


Fig. 2. Two-layer arbitrary anisotropic sphere with the inner radius $r_1 = 0.1$ m and the outer radius $r_2 = 0.2$ m embedded in a six-layer uniaxial background medium with a locally rough surface. The sphere straddles three planar layers.

reconstructed from the scattered fields \mathbf{E}_{sct} and \mathbf{H}_{sct} recorded at the receiver array. The problem is actually to search for the optimized $\bar{\chi}$ in (9) from measured data. In this work, we follow the similar VBIM procedure given in [28] to solve for the 12 unknown model parameters listed in (3). Since there is no difference between the assembly of the sensitivity matrix and the implementation of VBIM when the rough surface is present or absent and when the scatterers are placed inside one layer or across multiple layers as long as the DGFs are obtained, the computational complexity of the inversion process remains the same and we will not repeat the VBIM procedure here. Readers can refer to [28] for more details.

III. FORWARD VALIDATION

In this section, we validate the correctness of the forward EM scattering solver for 3-D arbitrary anisotropic scatterers placed across multiple subsurface planar layers with a locally rough surface by comparing the BCGS results with the FEM computation via the commercial software COMSOL. Meanwhile, we also compare the computational cost of the forward BCGS solver when the rough surface is present or absent. All the numerical simulations are performed on a workstation with a 44-core Intel Xeon 6161 2.2-G CPU and 1024-GB RAM. As shown in Fig. 2, a two-layer sphere with an inner radius $r_1 = 0.1$ m and an outer radius $r_2 = 0.2$ m straddles three planar layers of the background medium. The center of the sphere locates at (0, 0, 0) m. The interface between the top layer and the second layer is a 2-D locally Gaussian random rough surface with the rms height $h = 0.1$ m and correlation lengths $l_x = l_y = 0.05$ m. Its horizontal sizes are $L_x \times L_y = 0.6 \times 0.6$ m. The background layer boundaries locate at $z = -0.8$ m, $z = -0.6$ m, $z = 0.0$ m, $z = 0.1$ m, and $z = 0.6$ m, respectively. The top layer is air and the permeability values of all the layers are the same as that of free space μ_0 . Therefore, the dielectric parameters of the six background layers are

$$\bar{\epsilon}_b^1 = \text{diag}\{1.0, 1.0, 1.0\}, \quad \bar{\sigma}_b^1 = \text{diag}\{0, 0, 0\} \text{ mS/m} \quad (17a)$$

$$\bar{\epsilon}_b^2 = \text{diag}\{3.5, 3.5, 4.0\}, \quad \bar{\sigma}_b^2 = \text{diag}\{1, 1, 2\} \text{ mS/m} \quad (17b)$$

$$\bar{\epsilon}_b^3 = \text{diag}\{2.0, 2.0, 1.5\}, \quad \bar{\sigma}_b^3 = \text{diag}\{1, 1, 2\} \text{ mS/m} \quad (17c)$$

$$\bar{\epsilon}_b^4 = \text{diag}\{2.5, 2.5, 1.8\}, \quad \bar{\sigma}_b^4 = \text{diag}\{3, 3, 2\} \text{ mS/m} \quad (17d)$$

$$\bar{\epsilon}_b^5 = \text{diag}\{3.0, 3.0, 2.0\}, \quad \bar{\sigma}_b^5 = \text{diag}\{4, 4, 3\} \text{ mS/m} \quad (17e)$$

$$\bar{\epsilon}_b^6 = \text{diag}\{4.0, 4.0, 2.5\}, \quad \bar{\sigma}_b^6 = \text{diag}\{2, 2, 4\} \text{ mS/m}. \quad (17f)$$

The inner sphere has the dielectric parameter

$$\bar{\epsilon}_{s1} = \text{diag}\{3.0, 3.0, 4.0\}, \quad \bar{\sigma}_{s1} = \text{diag}\{2, 2, 6\} \text{ mS/m} \quad (18)$$

and the outer sphere has the dielectric parameter

$$\bar{\epsilon}_{s2} = \text{diag}\{3.5, 3.5, 2.0\}, \quad \bar{\sigma}_{s2} = \text{diag}\{5, 5, 2\} \text{ mS/m}. \quad (19)$$

However, these are only uniaxial anisotropic. The principal axes of both the inner sphere and the outer sphere are supposed to align with the vertical \hat{z} -axis. In practice, they may deviate away. Therefore, in this work, we rotate the principal axes according to (3) of [46] to generate symmetrical full tensors. The rotation angles of inner sphere and outer sphere are $\phi_1 = 30^\circ$, $\phi_2 = 120^\circ$ and $\phi_1 = 90^\circ$, $\phi_2 = 60^\circ$, respectively. Consequently, the dielectric parameters of the inner sphere become

$$\bar{\epsilon}'_{s1} = \begin{bmatrix} 3.75 & 0.433 & 0.0 \\ 0.433 & 3.25 & 0.0 \\ 0.0 & 0.0 & 3.00 \end{bmatrix} \quad (20a)$$

$$\bar{\sigma}'_{s1} = \begin{bmatrix} 5.00 & 1.732 & 0.0 \\ 1.732 & 3.00 & 0.0 \\ 0.0 & 0.0 & 2.00 \end{bmatrix} \text{ mS/m} \quad (20b)$$

and those of the outer sphere become

$$\bar{\epsilon}'_{s2} = \begin{bmatrix} 3.219 & 0.162 & -0.562 \\ 0.162 & 3.406 & 0.325 \\ -0.562 & 0.325 & 2.375 \end{bmatrix} \quad (21a)$$

$$\bar{\sigma}'_{s2} = \begin{bmatrix} 4.438 & 0.325 & -1.125 \\ 0.325 & 4.813 & 0.650 \\ -1.125 & 0.650 & 2.750 \end{bmatrix} \text{ mS/m}. \quad (21b)$$

The source is a unit electric dipole polarized at the direction of (1, 1, 1) and locates at $(x_s, y_s, z_s) = (0, 0, -1.3)$ m. The operation frequency is 1 GHz. The scattered fields are recorded by a 6×6 receiver array locating at the $z = -1.3$ m xy plane. The increment intervals between two adjacent receivers in both the \hat{x} - and \hat{y} -directions are 0.1 m. The coordinate of the first receiver is $(-0.25, -0.25, -1.3)$ m. The computational domain D enclosing the two-layer sphere has the dimensions of $0.44 \times 0.44 \times 0.44$ m and is discretized into $44 \times 44 \times 44$ voxels. The size of each voxel is $\Delta x \times \Delta y \times \Delta z = 0.01 \times 0.01 \times 0.01$ m.

Now, let us compare the incident electric fields and the total electric fields inside the computational domain D and the scattered fields at the receiver array when the rough surface is present or absent. We choose $4 \times 4 \times 4$ uniformly distributed sampling points with the spatial step of 0.1 m inside the domain D for comparisons. As shown in Fig. 3, all three field components in these 64 sampling points show good matches between the BCGS results and FEM results. The relative error is 4.89% when the rough surface is present but becomes 4.02% when it is absent. We then compare the total electric fields in the same sampling points. As shown in Fig. 4, their variation

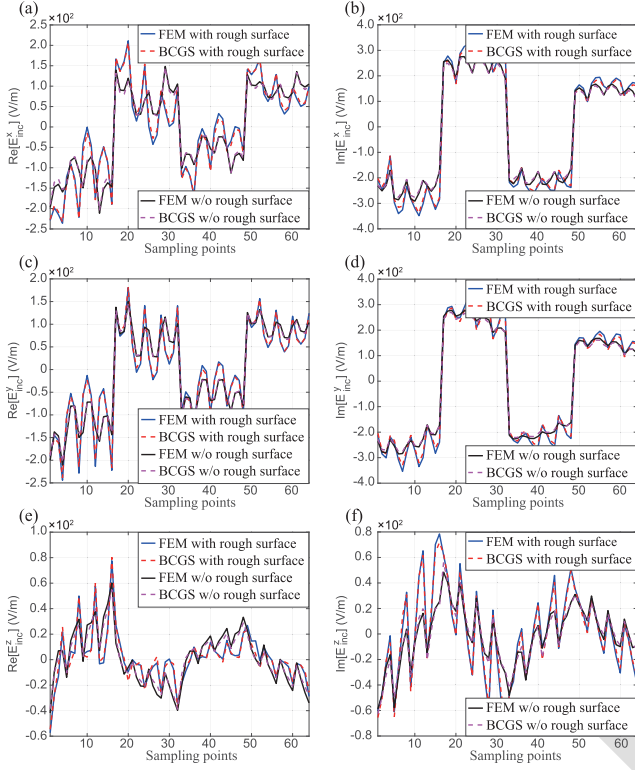


Fig. 3. Comparisons of the incident electric fields inside the computational domain enclosing the two-layer sphere computed by the BCGS and simulated by FEM when the rough surface is present or absent. (a) Real part of E_{inc}^x . (b) Imaginary part of E_{inc}^x . (c) Real part of E_{inc}^y . (d) Imaginary part of E_{inc}^y . (e) Real part of E_{inc}^z . (f) Imaginary part of E_{inc}^z .

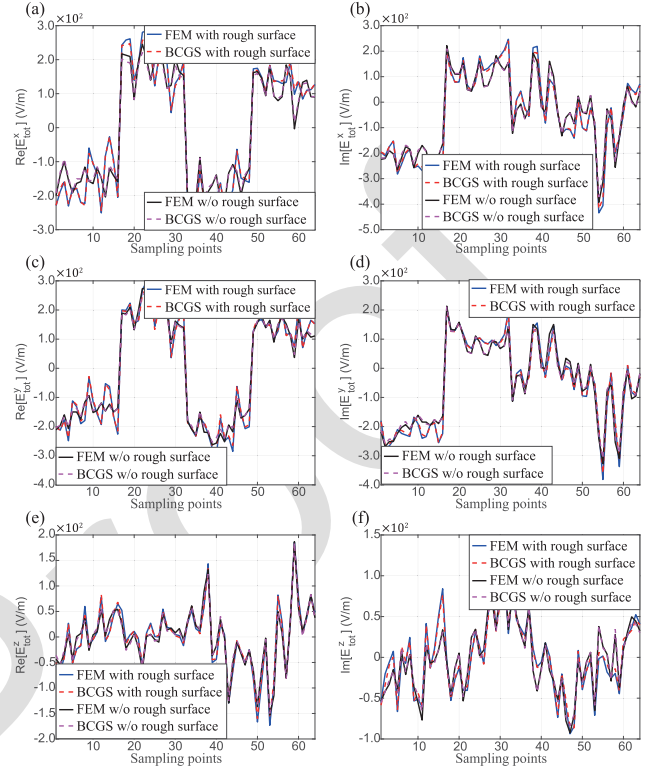


Fig. 4. Comparisons of the total electric fields inside the computational domain enclosing the two-layer sphere computed by the BCGS and simulated by FEM when the rough surface is present or absent. (a) Real part of E_{tot}^x . (b) Imaginary part of E_{tot}^x . (c) Real part of E_{tot}^y . (d) Imaginary part of E_{tot}^y . (e) Real part of E_{tot}^z . (f) Imaginary part of E_{tot}^z .

trends solved by BCGS and FEM also show good matches. The relative errors are 4.99% and 5.80% for the rough surface and flat surface scattering, respectively. Finally, we separately select four representative components of the scattered electric fields and the scattered magnetic fields to further verify the computation accuracy of our BCGS method. The scattered electric fields and magnetic fields at the receiver array are computed by (9) after the total electric fields are obtained. Fig. 5(a)–(d) shows the comparisons of several representative components of the scattered electric fields, and Fig. 5(e)–(h) shows the comparisons of representative scattered magnetic components. We can see that in most receivers the scattered fields solved by our BCGS method match well with the FEM results no matter for the cases with or without the rough surface although in a few receivers there still exist slight errors. Note the imaginary parts of E_{sct}^x , E_{sct}^y , H_{sct}^x , and H_{sct}^y have similar matches and are not shown here due to the space limitation. The relative errors of scattered electric fields and scattered magnetic fields are 3.89% and 4.25%, respectively, when the rough surface is present while they become 3.41% and 3.57%, respectively, when the rough surface is replaced with a flat one. The above comparisons indicate that our BCGS method can reliably solve the 3-D EM scattering problems for arbitrary anisotropic scatterers buried in a planarly uniaxial anisotropic layered medium with a locally rough surface.

We then compare the computational cost of the forward solver when the rough surface is present or absent.

TABLE I
MEMORY COST (GB) OF THE FORWARD SOLVER FOR DIFFERENT COMPUTATIONAL VARIABLES AND STAGES

	$\overline{\mathbf{G}}_{\mathbf{EJ}}^{it} \& \mathbf{E}_{inc}$	$\overline{\mathbf{G}}_{\mathbf{EJ}}^{ii}$	BCGS	$\overline{\mathbf{G}}_{\mathbf{E/HJ}}^{ri} \& \mathbf{E}_{sct} \& \mathbf{H}_{sct}$
w/o rough surface	0.002	1.006	1.024	0.891
with rough surface	23.35	521.6	498.3	23.20

TABLE II
COMPUTATION TIME OF THE FORWARD SOLVER FOR DIFFERENT COMPUTATIONAL VARIABLES AND STAGES

	$\overline{\mathbf{G}}_{\mathbf{EJ}}^{it} \& \mathbf{E}_{inc}$	$\overline{\mathbf{G}}_{\mathbf{EJ}}^{ii}$	BCGS	$\overline{\mathbf{G}}_{\mathbf{E/HJ}}^{ri} \& \mathbf{E}_{sct} \& \mathbf{H}_{sct}$
w/o rough surface	6.5 s	10.1 s	6.3 s	11.9 min
with rough surface	0.98 h	6.77 h	12.9 min	10.6 min

The memory cost is listed in Table I, and the computation time is listed in Table II. An intuitive feeling is that the computational cost of the forward solver when we consider the rough surface scattering is much higher compared with the situation only dealing with the planarly multilayered background medium. For example, for the computation of $\overline{\mathbf{G}}_{\mathbf{EJ}}^{it}$ and \mathbf{E}_{inc} , the forward solver including the rough surface effect needs up to 1100 times memory more than the solver for the purely planar background medium. The computation time discrepancy is also more than 500 times. This is mainly because the computation of $\overline{\mathbf{G}}_{\mathbf{EJ}}^{it}$ for the layered medium with

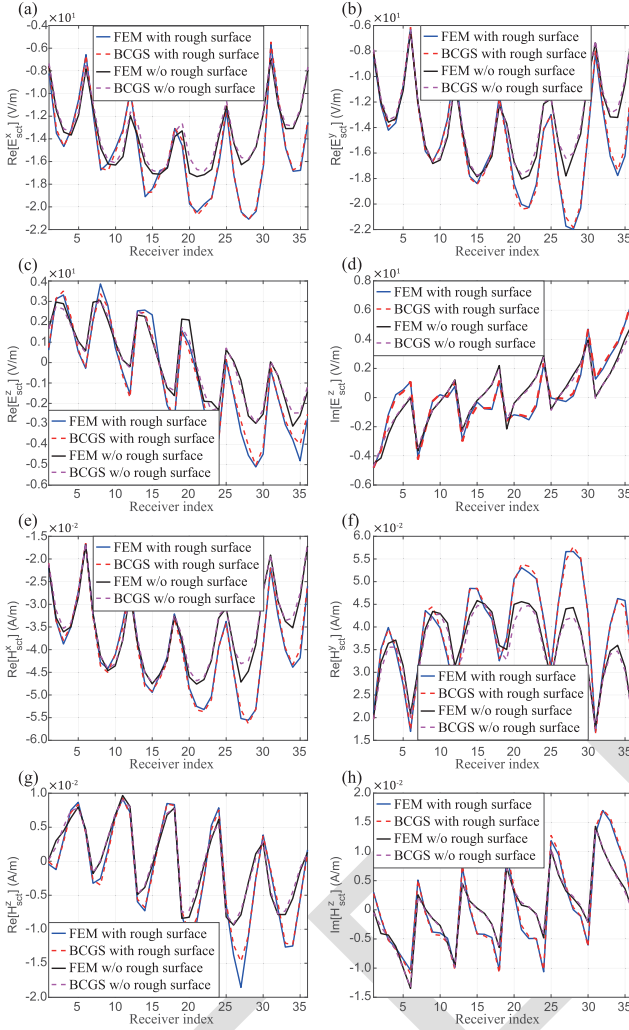


Fig. 5. Comparisons of representative scattered electric fields and magnetic fields at the receiver array computed by the BCGS and simulated by FEM when the rough surface is present or absent. (a) Real part of E_{sct}^x . (b) Imaginary part of E_{sct}^x . (c) Real part of E_{sct}^y . (d) Imaginary part of E_{sct}^y . (e) Real part of H_{sct}^x . (f) Imaginary part of H_{sct}^x . (g) Real part of H_{sct}^y . (h) Imaginary part of H_{sct}^y .

a rough surface needs to solve integral equations, e.g., (14) in this work, which increases both the computation time and memory cost. The discrepancy for the computational cost of $\bar{\bar{\mathbf{G}}}_{\mathbf{E}\mathbf{J}}^{ii}$ between the situations with and without the rough surface is almost the most significant one among the four items listed in Tables I and II. There are two reasons for this big discrepancy. The first one is that the computation of $\bar{\bar{\mathbf{G}}}_{\mathbf{E}\mathbf{J}}^{ii}$ still needs to solve the integral equations. The second reason is that the dimension of $\bar{\bar{\mathbf{G}}}_{\mathbf{E}\mathbf{J}}^{ii}$ for the purely planar layers is much smaller than that for the rough surface due its shift invariance in the xy plane. This also influences the computational cost of the BCGS solver. As shown in Tables I and II, the BCGS needs much more time and memory when EM scattering from the rough surface is considered. When the rough surface is present, the BCGS directly uses MoM. In contrast, when the rough surface is replaced with a flat one, BCGS uses FFT acceleration in the xy plane. One should note that

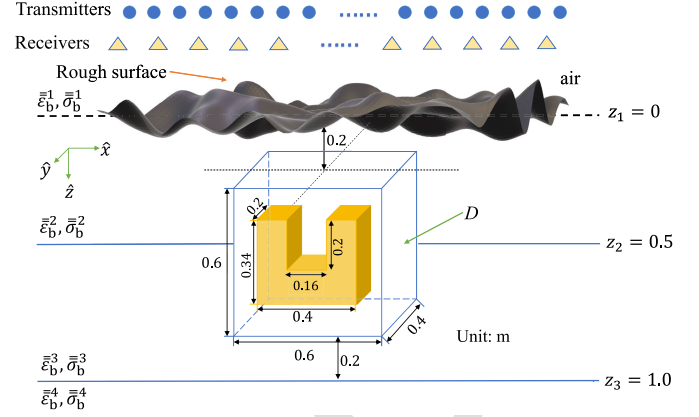


Fig. 6. Configuration of the inversion model with a 3-D homogeneous but arbitrary anisotropic “U”-shaped scatterer buried beneath the 2-D rough surface. The scatterer straddles the second and third layers. Its geometry sizes are annotated in the figure.

the computation time of the scattered fields has no obvious difference for the rough surface and flat surface scenarios. This is because some auxiliary matrices such as $\bar{\bar{\mathbf{G}}}_0^{bo,bo}$ used to solve for $\bar{\bar{\mathbf{G}}}^i$ in the integral equations have been used to compute $\bar{\bar{\mathbf{G}}}^i$ and $\bar{\bar{\mathbf{G}}}^{ii}$ and thus are directly ready when we compute $\bar{\bar{\mathbf{G}}}^i$. The last important point that must be mentioned here is the comparison to the computational cost of the commercial software COMSOL. Numerical experiments show that COMSOL needs 10.1 min to accomplish the simulation when the rough surface is absent but 11.2 min when the rough surface is present. It consumes 57.2-GB memory when the rough surface is absent but 66.1-GB memory when the rough surface is present. Compared with the data listed in Tables I and II, the FEM adopted by COMSOL definitely outperforms our BCGS when the rough surface is present. The major reason is that the evaluation of $\bar{\bar{\mathbf{G}}}_{\mathbf{E}\mathbf{J}}^{ii}$ takes too much resource when BOA is adopted.

IV. INVERSION ASSESSMENT

In this section, we assess the reconstruction ability of the VBIM solver for a 3-D arbitrary anisotropic object straddling multiple uniaxial planar layers beneath a 2-D rough surface. Meanwhile, the necessity to consider the rough surface in the inversion is validated. In other words, we quantitatively compare the reconstruction errors when the inversion model only considers the flat surface and when it includes the rough surface if the true model includes the rough surface. As shown in Fig. 6, a “U”-shaped anisotropic scatterer is placed across the second and third layers. Its 12 known parameters will be reconstructed simultaneously. The dimensions of the inversion domain D and the homogeneous scatterer are annotated in the figure. The true dielectric parameters of the “U”-shaped scatterer are listed in the second row of Table III. We use different rms height h values but the same correlation length $l_x = l_y = 0.1$ m to generate different 2-D Gaussian random rough surfaces. The background medium includes four layers and the boundary positions locate at $z = 0$ m, $z = 0.5$ m, and $z = 1.0$ m, respectively. The top layer is air and it is

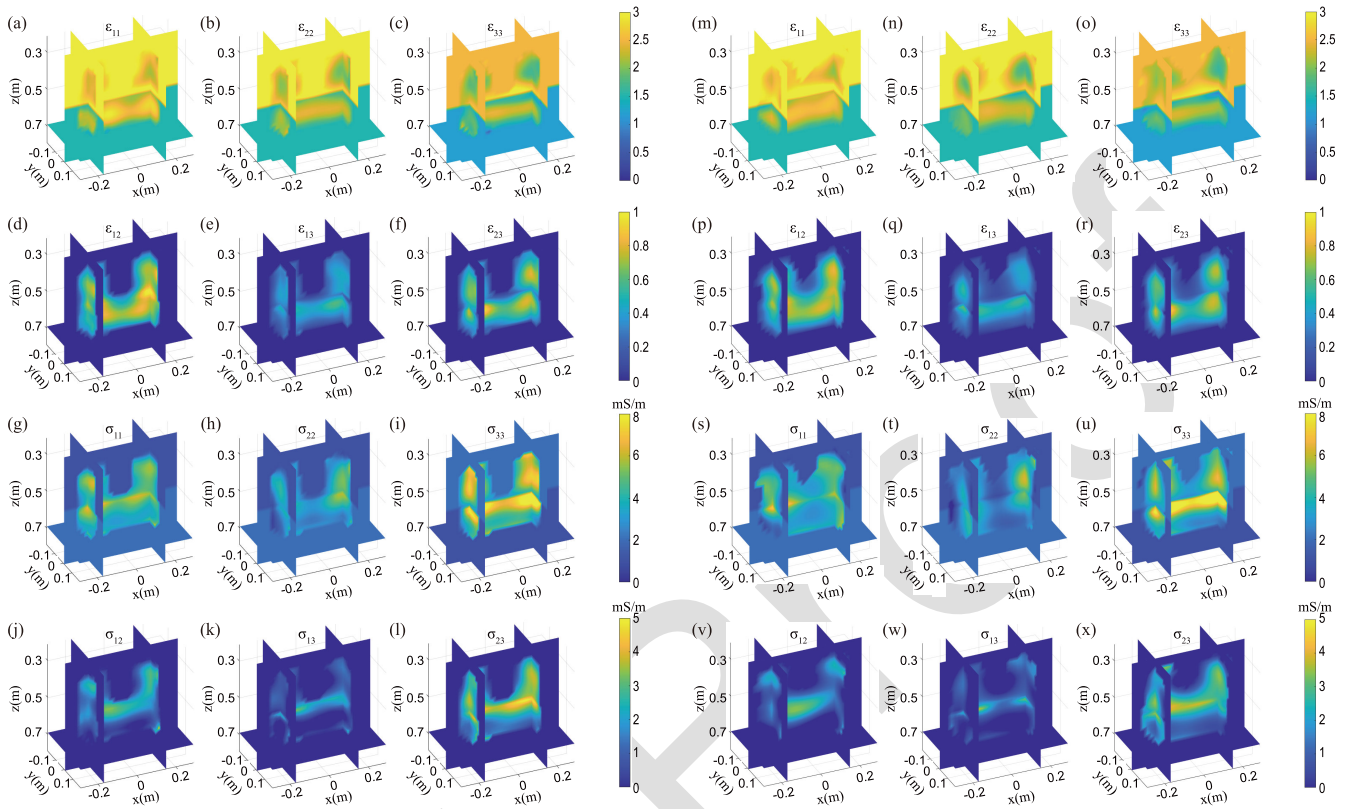


Fig. 7. Reconstructed 3-D distribution of 12 anisotropic parameters of the “U”-shaped scatterer straddling two subsurface layers when (a)–(l) noise-free and (m)–(x) 30-dB noise is added. The same 2-D rough surface is used in the forward and inversion models.

separated from the second layer by the 2-D rough surface. The other three planar layers are uniaxial anisotropic media which have the dielectric parameters

$$\bar{\epsilon}_b^2 = \text{diag}\{3.0, 3.0, 2.5\}, \quad \bar{\sigma}_b^2 = \text{diag}\{1, 1, 2\} \text{ mS/m} \quad (22a)$$

$$\bar{\epsilon}_b^3 = \text{diag}\{1.5, 1.5, 1.2\}, \quad \bar{\sigma}_b^3 = \text{diag}\{2, 2, 1\} \text{ mS/m} \quad (22b)$$

$$\bar{\epsilon}_b^4 = \text{diag}\{2.0, 2.0, 1.5\}, \quad \bar{\sigma}_b^4 = \text{diag}\{2, 2, 3\} \text{ mS/m}. \quad (22c)$$

Totally, 8×8 transmitters are uniformly placed in a 2.8×2.8 m square at $z = -0.3$ m. The increment between two adjacent transmitters in both the \hat{x} - and \hat{y} -directions is 0.4 m. The coordinate of the first transmitter is $(-1.4, -1.4, -0.3)$ m. Each transmitter is a unit dipole operating at 300 MHz and polarized at the direction of $(1, 1, 1)$. The scattered fields are recorded by a 9×9 receiver array which locates in the $z = -0.2$ m plane. The increment between two adjacent receivers in both the \hat{x} - and \hat{y} -directions is 0.45 m. The coordinate of the first receiver is $(-1.8, -1.8, -0.2)$ m. The inversion domain D enclosing the “U”-shaped scatterer has the dimensions of $0.6 \times 0.4 \times 0.6$ m and its center locates at $(0, 0, 0.5)$ m. It is discretized into $30 \times 20 \times 30$ voxels, and the size of each voxel is $\Delta x = \Delta y = \Delta z = 0.02$ m. The measured scattered field data recorded at the receiver array are simulated by the BCGS forward solver which has been validated in Section III. The model misfit defined in (16) of [47] is used to indicate the inversion performance. In addition, the structural consistency constraint presented in [35] is used to filter out the background clutter in the inversion.

First, let us validate the inversion performance of the VBIM solver when the rough surface has large fluctuations. We set its rms height $h = 0.1$ m in the forward model. The exact same rough surface is included in the inversion model. Fig. 7 shows the reconstructed relative permittivity and conductivity profiles for both the diagonal and off-diagonal elements. Fig. 8 shows their 2-D slices in different directions or positions for both the noise-free and 30-dB noise cases. Note we add 30-dB white Gaussian noise to the simulated scattered field data to test the antinoise ability of the VBIM solver. Here, the noise level is defined according to the signal-to-noise ratio (SNR) of power. Numerical simulations show that the VBIM solver takes 17 iterations and 19.5 h to complete the inversion when noise-free while it takes seven iterations and 7.6 h to complete the inversion when 30-dB noise is added. We can see that the reconstructed 3-D shapes of different elements shown in Fig. 7(a)–(l) are close to the true “U” shape, which is further confirmed by the good matches between the reconstructed 2-D slices and the white dotted boxes shown in Fig. 8(a)–(l). In addition, the mean values of the inverted dielectric parameters listed in the third row of Table III are also close to their true values. The corresponding model misfits are listed in the second row of Table IV. When 30-dB noise is added to the scattered field data, the reconstructed shapes have some distortion, as shown in Figs. 7(m)–(x) and 8(m)–(x). Especially the protrusions are severely distorted. On the other hand, the mean values of the reconstructed 12 dielectric parameters listed in the fourth row of Table III show obvious larger discrepancies with respect to

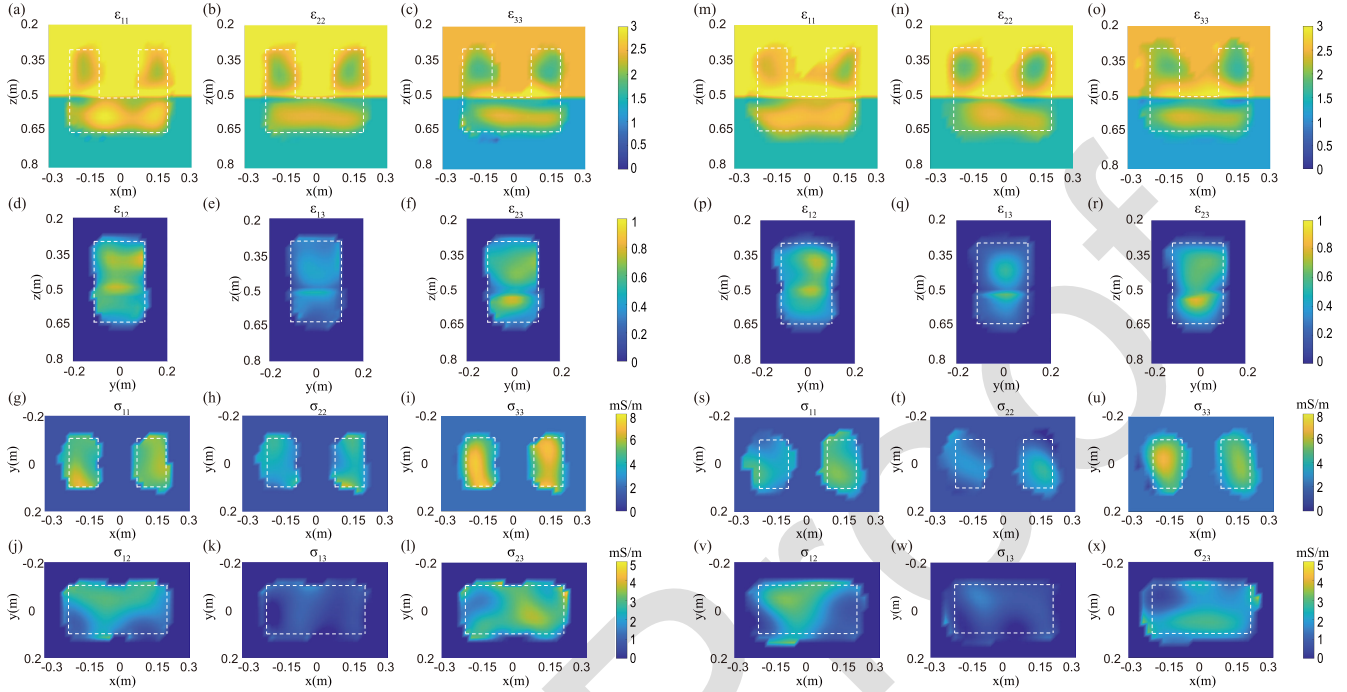


Fig. 8. Reconstructed xz slices of the relative permittivity profiles for diagonal elements at $y = 0$ when (a)–(c) noise-free and (m)–(o) 30-dB noise is added. Reconstructed yz slices of the relative permittivity profiles for off-diagonal elements at $x = -0.17$ m when (d)–(f) noise-free and (p)–(r) 30-dB noise is added. Reconstructed xy slices of the conductivity profiles for diagonal elements at $z = 0.25$ m when (g)–(i) noise-free and (s)–(u) 30-dB noise is added. Reconstructed xy slices of the conductivity profiles for off-diagonal elements at $z = 0.45$ m when (j)–(l) noise-free and (v)–(x) 30-dB noise is added. The same 2-D rough surface is used in the forward and inversion models. The white dotted boxes denote true shapes.

TABLE III

TRUE AND MEAN RECONSTRUCTED DIELECTRIC PARAMETER VALUES OF THE ANISOTROPIC “U” SHAPE IN THE RECONSTRUCTION

Models	Parameters	ϵ_{11}	ϵ_{22}	ϵ_{33}	ϵ_{12}	ϵ_{13}	ϵ_{23}	σ_{11}	σ_{22}	σ_{33}	σ_{12}	σ_{13}	σ_{23}
Ground truth		2.50	2.20	2.00	0.70	0.40	0.60	5.0	4.0	7.0	2.0	1.0	3.0
$h_{true} = 0.1$ m; $h_{inv} = 0.1$ m; noise free		2.43	2.20	2.01	0.54	0.30	0.46	4.2	3.3	5.3	1.5	0.7	2.2
$h_{true} = 0.1$ m; $h_{inv} = 0.1$ m; 30 dB noise		2.43	2.25	2.02	0.41	0.23	0.35	3.5	2.8	4.4	1.1	0.6	1.7
$h_{true} = 0.1$ m; $h_{inv} = 0.0$ m; noise free		2.19	2.10	1.92	0.40	0.33	0.35	3.6	3.3	4.0	1.8	1.9	2.0
$h_{true} = 0.02$ m; $h_{inv} = 0.02$ m; noise free		2.44	2.20	2.01	0.55	0.31	0.46	4.3	3.4	5.3	1.5	0.7	2.2
$h_{true} = 0.02$ m; $h_{inv} = 0.0$ m; noise free		2.35	2.20	2.07	0.45	0.25	0.39	3.8	3.0	4.7	1.5	1.0	1.8
$h_{true} = 0.0$ m; $h_{inv} = 0.0$ m; noise free		2.44	2.20	2.01	0.55	0.31	0.46	4.3	3.4	5.3	1.5	0.7	2.2

Remark: the unit of σ is mS/m; h_{true} denotes the RMS height of the true rough surface while h_{inv} denotes the RMS height used in the inversion; when the RMS height becomes zero, the rough surface degenerates into a flat one.

their true values compared with those obtained when noise-free. This is also confirmed by the larger model misfit values listed in the third row of Table IV. Notwithstanding, both the reconstructed general “U” shape and the inverted diagonal elements of the relative permittivity are still close to their ground truths.

Then, we perform a series of numerical experiments to testify to the necessity to include the rough surface in the inversion. We just choose three representative components, i.e., ϵ_{11} , σ_{22} , and σ_{23} show the reconstructed slices in Fig. 9. For convenience, we use h_{true} to denote the rms height of the rough surface in the true model and h_{inv} to denote its value used in the inversion. When they have the same value, the rough surfaces are also the same in our work. Note when h becomes zero, the rough surface degenerates into a flat one. As shown in Fig. 9(a)–(c), (g)–(i), and (m)–(o), when the surface shapes used in the inversion are the same as their true shapes, the reconstructed profiles are close to each other,

no matter how large the fluctuations of the rough surfaces are. This is further confirmed by the corresponding mean reconstructed parameter values and the model misfit values listed in Tables III and IV. That is to say, the VBIM solver is reliable as long as the rough surface is precisely modeled in the inversion process. The influence of the rough surface is only manifested in the computational cost of the forward BCGS solver. Its effect on the inversion results is negligible. Now, let us discuss the inversion performance if we neglect the rough surface in inversion. In other words, we only use the flat surface in the inversion but the true model has a fluctuation one. Fig. 9(d)–(f) and (j)–(l) shows the VBIM inversion results when $h_{true} = 0.1$ m and $h_{true} = 0.02$ m, respectively. Obviously, larger rms height leads to larger distortion of the reconstructed profiles, which is also confirmed by the corresponding obtained mean values and the model misfit values listed in Tables III and IV. When the rms height is 0.02 m, we can still discern the basic shapes of the reconstructed

TABLE IV
MODEL MISFIT VALUES (%) FOR THE RECONSTRUCTION OF THE ANISOTROPIC “U” SHAPE

Parameters	ϵ_{11}	ϵ_{22}	ϵ_{33}	ϵ_{12}	ϵ_{13}	ϵ_{23}	σ_{11}	σ_{22}	σ_{33}	σ_{12}	σ_{13}	σ_{23}
Models												
$h_{true} = 0.1$ m; $h_{inv} = 0.1$ m; noise free	5.87	5.65	7.64	41.3	42.2	42.5	27.9	25.3	33.7	62.5	88.3	51.9
$h_{true} = 0.1$ m; $h_{inv} = 0.1$ m; 30 dB noise	6.83	6.85	8.59	47.8	50.4	48.4	38.2	32.5	39.6	79.6	98.8	66.2
$h_{true} = 0.1$ m; $h_{inv} = 0.0$ m; noise free	25.4	26.5	30.6	113	156	116	87.9	102	79.9	186	382	139
$h_{true} = 0.02$ m; $h_{inv} = 0.02$ m; noise free	5.97	5.69	7.43	41.0	42.1	42.6	28.4	25.5	33.8	61.3	84.4	52.2
$h_{true} = 0.02$ m; $h_{inv} = 0.0$ m; noise free	12.1	12.2	13.2	59.1	69.5	66.9	57.4	50.1	52.5	121	183	84.6
$h_{true} = 0.0$ m; $h_{inv} = 0.0$ m; noise free	5.95	5.66	7.37	41.4	42.6	42.8	28.5	25.4	34.3	60.5	85.5	52.8

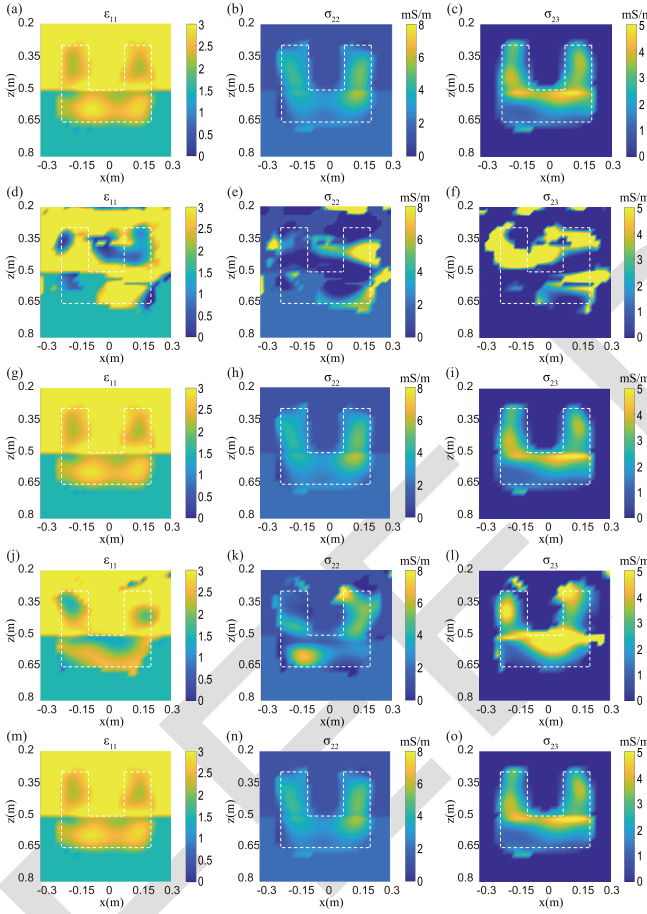


Fig. 9. Reconstructed xz slices at $y = 0$ for three representative components when (a)–(c) $h_{true} = 0.1$ m and $h_{inv} = 0.1$ m, (d)–(f) $h_{true} = 0.1$ m and $h_{inv} = 0.0$ m, (g)–(i) $h_{true} = 0.02$ m and $h_{inv} = 0.02$ m, (j)–(l) $h_{true} = 0.02$ m and $h_{inv} = 0.0$ m, and (m)–(o) $h_{true} = 0.0$ m and $h_{inv} = 0.0$ m, respectively. Only the noise-free results are shown here. The white dotted boxes denote true shapes.

profiles, although they are even worse than the profiles from the inversion with 30-dB noise, as shown in Fig. 8(m)–(x). However, when the rms height increases to 0.1 m, the “U” shape is no longer discernible, as shown in Fig. 9(d)–(f).

Finally, it should be emphasized that the model misfits of the inverted permittivity diagonal elements are obviously smaller than those of off-diagonal elements. This is due to two reasons. The first one is that the diagonal elements of the relative permittivity tensor are larger than the off-diagonal elements. As a result, the VBIM solver is more sensitive to the variations in the diagonal elements. The second one

is that the off-diagonal elements of the relative permittivity tensor of the background medium are zero. Therefore, the denominators in the model misfit computation are rather small (see (16) of [47]), which causes large model misfit values. Larger model misfits of the conductivity compared with those of the permittivity listed in Table IV are also caused by similar reasons.

V. CONCLUSION

In this article, we solve the 3-D forward and inverse scattering problems for arbitrary anisotropic objects straddling multiple planar uniaxial layers which are covered by a 2-D locally rough surface. To account for the EM scattering from the rough surface, we use the BOA to divide the 2-D rough surface into several fictitious 3-D scatterers embedded inside the first planar layer and the second one. Then the integral equation method is adopted to solve for the DGFs of the uniaxial anisotropic background medium. Finally, the BCGS is used to solve the EM scattering from the subsurface 3-D anisotropic objects and VBIM is used to simultaneously reconstruct multiple anisotropic parameters of the scatterer. The computation precision of the forward BCGS solver is authenticated by comparing its solutions of incident fields, total fields inside the computational domain, and the scattered fields at the receiver array with the FEM simulation results. The VBIM solver is also tested to simultaneously reconstruct 12 anisotropic parameters of a subsurface 3-D scatterer which straddles multiple planar layers beneath a rough surface and has an electrical size of less than one wavelength.

On the other hand, we have studied the influence of the rough surface on both the forward and inverse scattering computation. In the forward process, the rough surface leads to significantly increased memory cost and computation time. There are two reasons. The first one is that acquiring DGFs when the rough surface is present needs solving additional integral equations while only the transmission-line analogy method is adopted when the rough surface is absent. The second reason lies in the implementation of the BCGS algorithm. When the rough surface is present, the shift invariance of the DGFs in the horizontal xy plane becomes invalid. This increases both the implementation time and memory of the BCGS solver. One feasible way to lower the computational cost for the evaluation of DGFs is replacing the volume integration with the surface integration in BOA. Note each fictitious buried object to simulate the rough surface is actually a homogeneous one. Therefore, we can directly discretize

its surface and adopt the surface integral equation instead of the volume integral equation to significantly reduce the unknowns. Of course, this improved method will be left as our future work and will not be discussed in detail here. In the inversion process, the necessity to include the rough surface is testified to. It is found that the reconstructed 12 anisotropic dielectric parameters show little difference for different surface fluctuations as long as the accurate rough surface of the true model is used in the inversion, even when the rough surface has a large rms value. However, the reconstructed profiles show obvious distortions if a flat surface replaces the rough one in the inversion.

APPENDIX

The DGFs in a planarly uniaxial multilayered medium is evaluated based on the transmission-line analogy method [38]. The spatial-domain DGFs are computed from the spectral-domain ones based on 2-D inverse Fourier transforms

$$\bar{\bar{\mathbf{G}}}_{\mathbf{E}\mathbf{J}}(\mathbf{r}, \mathbf{r}') = \frac{1}{4\pi^2} \iint_{-\infty}^{+\infty} \tilde{\mathbf{G}}_{\mathbf{E}\mathbf{J}}(\mathbf{k}_\rho; z, z') e^{-j\mathbf{k}_\rho \cdot \boldsymbol{\rho}} d\mathbf{k}_x d\mathbf{k}_y \quad (\text{A1a})$$

$$\bar{\bar{\mathbf{G}}}_{\mathbf{H}\mathbf{J}}(\mathbf{r}, \mathbf{r}') = \frac{1}{4\pi^2} \iint_{-\infty}^{+\infty} \tilde{\mathbf{G}}_{\mathbf{H}\mathbf{J}}(\mathbf{k}_\rho; z, z') e^{-j\mathbf{k}_\rho \cdot \boldsymbol{\rho}} d\mathbf{k}_x d\mathbf{k}_y \quad (\text{A1b})$$

where

$$\begin{aligned} \tilde{\mathbf{G}}_{\mathbf{E}\mathbf{J}} &= \left(-\frac{k_x^2}{k_\rho^2} V_i^e - \frac{k_y^2}{k_\rho^2} V_i^h \right) \hat{x}\hat{x} + \left(-\frac{k_x k_y}{k_\rho^2} V_i^e + \frac{k_x k_y}{k_\rho^2} V_i^h \right) \hat{x}\hat{y} \\ &+ \left(-\frac{k_y^2}{k_\rho^2} V_i^e - \frac{k_x^2}{k_\rho^2} V_i^h \right) \hat{y}\hat{y} + \left(-\frac{k_x k_y}{k_\rho^2} V_i^e + \frac{k_x k_y}{k_\rho^2} V_i^h \right) \hat{y}\hat{x} \\ &+ \left(\frac{k_x}{\omega \epsilon_0 \epsilon'_{33}} V_v^e \right) \hat{x}\hat{z} + \left(\frac{k_y}{\omega \epsilon_0 \epsilon'_{33}} V_v^e \right) \hat{y}\hat{z} + \left(\frac{k_x}{\omega \epsilon_0 \epsilon'_{33}} I_i^e \right) \hat{z}\hat{x} \\ &+ \left(\frac{k_y}{\omega \epsilon_0 \epsilon'_{33}} I_i^e \right) \hat{z}\hat{y} + \left(-\frac{k_\rho^2}{\omega^2 \epsilon_0^2 \epsilon'_{33} \epsilon'_{33}} I_v^e \right) \hat{z}\hat{z} \end{aligned} \quad (\text{A2a})$$

$$\begin{aligned} \tilde{\mathbf{G}}_{\mathbf{H}\mathbf{J}} &= \left(-\frac{k_x k_y}{k_\rho^2} I_i^h + \frac{k_x k_y}{k_\rho^2} I_i^e \right) \hat{x}\hat{x} + \left(\frac{k_x^2}{k_\rho^2} I_i^h + \frac{k_y^2}{k_\rho^2} I_i^e \right) \hat{x}\hat{y} \\ &+ \left(\frac{k_x k_y}{k_\rho^2} I_i^h - \frac{k_x k_y}{k_\rho^2} I_i^e \right) \hat{y}\hat{y} + \left(-\frac{k_y^2}{k_\rho^2} I_i^h - \frac{k_x^2}{k_\rho^2} I_i^e \right) \hat{y}\hat{x} \\ &+ \left(-\frac{k_y}{\omega \epsilon_0 \epsilon'_{33}} I_v^e \right) \hat{x}\hat{z} + \left(\frac{k_x}{\omega \epsilon_0 \epsilon'_{33}} I_v^e \right) \hat{y}\hat{z} + \left(\frac{k_y}{\omega \mu_0 \mu'_{33}} V_i^h \right) \hat{z}\hat{x} \\ &+ \left(-\frac{k_x}{\omega \mu_0 \mu'_{33}} V_i^h \right) \hat{z}\hat{y} \end{aligned} \quad (\text{A2b})$$

in which the voltage and current terms are actually the plane wave harmonics and their expressions can be found in Section V of [48]. The superscript h stands for the transverse electric (TE) mode, while e stands for the transverse magnetic (TM) mode. The ϵ'_{33} means the permittivity value is taken from the layer in which the source point \mathbf{r}' locates.

The 2-D inverse Fourier transform in (A1) can be further simplified by

$$\begin{aligned} &\frac{1}{4\pi^2} \iint_{-\infty}^{+\infty} \frac{\cos n\xi}{\sin n\phi} \tilde{f}(k_\rho) e^{-j\mathbf{k}_\rho \cdot \boldsymbol{\rho}} d\mathbf{k}_x d\mathbf{k}_y \\ &= \frac{1}{2\pi} \int_0^{+\infty} \tilde{f}(k_\rho) k_\rho dk_\rho \frac{1}{2\pi} \int_0^{2\pi} \frac{\cos n\xi}{\sin n\phi} e^{-j k_\rho \rho \cos(\xi - \phi)} d\xi \\ &= (-j)^n \frac{\cos n\phi}{\sin n\phi} \cdot \frac{1}{2\pi} \int_0^{+\infty} \tilde{f}(k_\rho) J_n(k_\rho \rho) k_\rho dk_\rho \end{aligned} \quad (\text{A3})$$

which is the famous Sommerfeld integration, and J_n is the Bessel function of the n th order. ξ is the angle between the vector $\mathbf{k}_\rho = \hat{x}k_x + \hat{y}k_y$ and the \hat{x} -axis, while ϕ is the angle between the vector $\boldsymbol{\rho} = \hat{x}(x - x') + \hat{y}(y - y')$ and the \hat{x} -axis. The fast numerical computation of the Sommerfeld integration can be found in [49].

When the source point and the field point locate inside the same layer, the DGF includes two parts, the primary field and the contribution from the layer boundary reflection. For a 3-D uniaxial anisotropic medium, the primary field of $\bar{\bar{\mathbf{G}}}_{\mathbf{E}\mathbf{J}}$ has the analytical solution and its expression can be found in Appendix A of [25]. Obviously, $\bar{\bar{\mathbf{G}}}_{\mathbf{E}\mathbf{J}}$ is singular when $\mathbf{r} = \mathbf{r}'$. In the integration equation, when the source point and the field point are overlapped at the center of a discretized cubic voxel with the volume of ΔV , the mean $\bar{\bar{\mathbf{G}}}_{\mathbf{E}\mathbf{J}}$ for an isotropic medium can be analytically evaluated via the sphere approximation method given in the Appendix of [50]. However, the method is no longer valid for a uniaxial anisotropic medium. Therefore, we compute the mean $\bar{\bar{\mathbf{G}}}_{\mathbf{E}\mathbf{J}}$ numerically. Specifically speaking, we can further discretize the cubic voxel into a series of smaller voxels, place the field point \mathbf{r} at the center of the cubic voxel and place a fictitious source point at the center of each smaller voxel, and finally compute the mean $\bar{\bar{\mathbf{G}}}_{\mathbf{E}\mathbf{J}}$ value. Another important issue is the contribution to the mean $\bar{\bar{\mathbf{G}}}_{\mathbf{E}\mathbf{J}}$ from the singular point $\mathbf{r} = \mathbf{r}'$ itself. In a homogeneous uniaxial medium, only the diagonal elements are not zero and they are evaluated as [51]

$$\begin{aligned} G_{EJ}^{xx} &= G_{EJ}^{yy} \\ &= \frac{j\omega\mu_0}{k^2\Delta V} \cdot \frac{1}{v^e} \left[\frac{1}{3} - \frac{2}{5} \left(\frac{1}{v^e} - 1 \right) + \frac{3}{7} \left(\frac{1}{v^e} - 1 \right)^2 + \dots \right] \end{aligned} \quad (\text{A4a})$$

$$G_{EJ}^{zz} = \frac{j\omega\mu_0}{k^2\Delta V} \cdot \left[\frac{1}{3} - \frac{1}{5} \left(\frac{1}{v^e} - 1 \right) + \frac{1}{7} \left(\frac{1}{v^e} - 1 \right)^2 + \dots \right] \quad (\text{A4b})$$

where $k = \omega\sqrt{\epsilon_0\mu_0}\sqrt{\epsilon_{11}\mu_{11}}$, and $v^e = \epsilon_{11}/\epsilon_{33}$ is in the neighborhood of 1. Obviously, (A4) degenerates into

$$\bar{\bar{\mathbf{G}}}_{\mathbf{E}\mathbf{J}} = \frac{j\omega\mu_0}{k^2\Delta V} \cdot \text{diag} \left\{ \frac{1}{3} \quad \frac{1}{3} \quad \frac{1}{3} \right\} \quad (\text{A5})$$

when the homogeneous medium becomes isotropic [52].

REFERENCES

- [1] X. Millard and Q. H. Liu, "Simulation of near-surface detection of objects in layered media by the BCGS-FFT method," *IEEE Trans. Geosci. Remote Sens.*, vol. 42, no. 2, pp. 327–334, Feb. 2004.

- [2] R. Chandra, H. Zhou, I. Balasingham, and R. M. Narayanan, "On the opportunities and challenges in microwave medical sensing and imaging," *IEEE Trans. Biomed. Eng.*, vol. 62, no. 7, pp. 1667–1682, Jul. 2015.
- [3] K. Yang, C. Torres-Verdin, and A. E. Yilmaz, "Detection and quantification of three-dimensional hydraulic fractures with horizontal borehole resistivity measurements," *IEEE Trans. Geosci. Remote Sens.*, vol. 53, no. 8, pp. 4605–4615, Aug. 2015.
- [4] B. Wu, "Electromagnetic analysis of massive vertical interconnects for dense pin assignment optimization using multiple scattering technique," in *Proc. IEEE Int. Symp. Electromagn. Compat. IEEE Asia-Pacific Symp. Electromagn. Compat. (EMC/APEMC)*, May 2018, pp. 963–965.
- [5] K. Donepudi, K. Gang, J. Song, and W. Chew, "Higher-order MoM implementation to solve integral equations," in *Proc. IEEE Antennas Propag. Soc. Int. Symp.*, vol. 3, Jul. 1999, pp. 1716–1719.
- [6] X. Min Xu and Q. H. Liu, "The BCGS-FFT method for electromagnetic scattering from inhomogeneous objects in a planarly layered medium," *IEEE Antennas Wireless Propag. Lett.*, vol. 1, pp. 77–80, 2002.
- [7] P. Zwamborn and P. M. van den Berg, "The three dimensional weak form of the conjugate gradient FFT method for solving scattering problems," *IEEE Trans. Microw. Theory Techn.*, vol. 40, no. 9, pp. 1757–1766, Sep. 1992.
- [8] Z. Q. Zhang and Q. H. Liu, "Three-dimensional weak-form conjugate and biconjugate-gradient FFT methods for volume integral equations," *Microw. Opt. Technol. Lett.*, vol. 29, no. 5, pp. 350–356, 2001.
- [9] N. Engheta, W. D. Murphy, V. Rokhlin, and M. S. Vassiliou, "The fast multipole method (FMM) for electromagnetic scattering problems," *IEEE Trans. Antennas Propag.*, vol. 40, no. 6, pp. 634–641, Jun. 1992.
- [10] J. Song, C.-C. Lu, and W. Cho Chew, "Multilevel fast multipole algorithm for electromagnetic scattering by large complex objects," *IEEE Trans. Antennas Propag.*, vol. 45, no. 10, pp. 1488–1493, Oct. 1997.
- [11] T. Xia, L. L. Meng, Q. S. Liu, H. H. Gan, and W. C. Chew, "A low-frequency stable broadband multilevel fast multipole algorithm using plane wave multipole hybridization," *IEEE Trans. Antennas Propag.*, vol. 66, no. 11, pp. 6137–6145, Nov. 2018.
- [12] K. Yang and A. E. Yilmaz, "A three-dimensional adaptive integral method for scattering from structures embedded in layered media," *IEEE Trans. Geosci. Remote Sens.*, vol. 50, no. 4, pp. 1130–1139, Apr. 2012.
- [13] Y. M. Wang and W. C. Chew, "An iterative solution of the two-dimensional electromagnetic inverse scattering problem," *Int. J. Imag. Syst. Technol.*, vol. 1, no. 1, pp. 100–108, 1989.
- [14] N. Zaiping, Y. Feng, Z. Yanwen, and Z. Yerong, "Variational born iteration method and its applications to hybrid inversion," *IEEE Trans. Geosci. Remote Sens.*, vol. 38, no. 4, pp. 1709–1715, Jul. 2000.
- [15] W. C. Chew and Y. M. Wang, "Reconstruction of two-dimensional permittivity distribution using the distorted born iterative method," *IEEE Trans. Med. Imag.*, vol. 9, no. 2, pp. 218–225, Jun. 1990.
- [16] P. M. V. D. Berg and R. E. Kleinman, "A contrast source inversion method," *Inverse Problems*, vol. 13, no. 6, pp. 1607–1620, Dec. 1997.
- [17] P. M. V. D. Berg, A. L. V. Broekhoven, and A. Abubakar, "Extended contrast source inversion," *Inverse Problems*, vol. 15, no. 5, pp. 1325–1344, Oct. 1999.
- [18] X. Chen, "Subspace-based optimization method for solving inverse-scattering problems," *IEEE Trans. Geosci. Remote Sens.*, vol. 48, no. 1, pp. 42–49, Jan. 2010.
- [19] Y. Liu et al., "A frequency-hopping subspace-based optimization method for reconstruction of 2-D large uniaxial anisotropic scatterers with TE illumination," *IEEE Trans. Geosci. Remote Sens.*, vol. 54, no. 10, pp. 6091–6099, Oct. 2016.
- [20] X. Ye and X. Chen, "Subspace-based distorted-born iterative method for solving inverse scattering problems," *IEEE Trans. Antennas Propag.*, vol. 65, no. 12, pp. 7224–7232, Dec. 2017.
- [21] T. Sarkar, E. Arvas, and S. Rao, "Application of FFT and the conjugate gradient method for the solution of electromagnetic radiation from electrically large and small conducting bodies," *IEEE Trans. Antennas Propag.*, vol. AP-34, no. 5, pp. 635–640, May 1986.
- [22] L. Zhuang, S. He, X. Ye, W. Hu, W. Yu, and G. Zhu, "The BCGS-FFT method combined with an improved discrete complex image method for EM scattering from electrically large objects in multilayered media," *IEEE Trans. Geosci. Remote Sens.*, vol. 48, no. 3, pp. 1180–1185, Mar. 2010.
- [23] Q. M. Nguyen, V. Dang, O. Kilic, and E. El-Araby, "Parallelizing fast multipole method for large-scale electromagnetic problems using GPU clusters," *IEEE Antennas Wireless Propag. Lett.*, vol. 12, pp. 868–871, 2013.
- [24] Y. Zhong, P.-P. Ding, M. Lambert, D. Lesselier, and X. Chen, "Fast calculation of scattering by 3-D inhomogeneities in uniaxial anisotropic multilayers," *IEEE Trans. Antennas Propag.*, vol. 62, no. 12, pp. 6365–6374, Dec. 2014.
- [25] J. Zhuo, F. Han, L. Ye, Z. Yu, and Q. H. Liu, "Simulation of electromagnetic scattering of 3-D inhomogeneous biaxial anisotropic magnetodielectric objects embedded in uniaxial anisotropic media by the mixed-order BCGS-FFT method," *IEEE Trans. Microw. Theory Techn.*, vol. 66, no. 8, pp. 3745–3755, Aug. 2018.
- [26] F. Han, J. Zhuo, N. Liu, Y. Liu, H. Liu, and Q. H. Liu, "Fast solution of electromagnetic scattering for 3-D inhomogeneous anisotropic objects embedded in layered uniaxial media by the BCGS-FFT method," *IEEE Trans. Antennas Propag.*, vol. 67, no. 3, pp. 1748–1759, Mar. 2019.
- [27] K. Yang and A. E. Yilmaz, "FFT-accelerated analysis of scattering from complex dielectrics embedded in uniaxial layered media," *IEEE Geosci. Remote Sens. Lett.*, vol. 10, no. 4, pp. 662–666, Jul. 2013.
- [28] J. Li, J. Zhuo, Z. Guan, F. Han, and Q. H. Liu, "3-D electromagnetic scattering and inverse scattering by magnetodielectric objects with arbitrary anisotropy in layered uniaxial media," *IEEE Trans. Antennas Propag.*, vol. 68, no. 2, pp. 1009–1022, Feb. 2020.
- [29] J. Wang, J. Li, Y. Chen, F. Han, and Q. H. Liu, "Simulation of 3-D electromagnetic scattering and inverse scattering by arbitrary anisotropic dielectric objects embedded in layered arbitrary anisotropic media," *IEEE Trans. Antennas Propag.*, vol. 68, no. 8, pp. 6473–6478, Aug. 2020.
- [30] T. Lan, N. Liu, Y. Liu, F. Han, and Q. H. Liu, "2-D electromagnetic scattering and inverse scattering from magnetodielectric objects based on integral equation method," *IEEE Trans. Antennas Propag.*, vol. 67, no. 2, pp. 1346–1351, Feb. 2019.
- [31] W. Zhang and Q. H. Liu, "Three-dimensional scattering and inverse scattering from objects with simultaneous permittivity and permeability contrasts," *IEEE Trans. Geosci. Remote Sens.*, vol. 53, no. 1, pp. 429–439, Jan. 2015.
- [32] T. Jun Cui, W. Cho Chew, A. A. Aydin, and S. Chen, "Inverse scattering of two-dimensional dielectric objects buried in a lossy earth using the distorted born iterative method," *IEEE Trans. Geosci. Remote Sens.*, vol. 39, no. 2, pp. 339–346, Feb. 2001.
- [33] T. Jun Cui, Y. Qin, Y. Ye, J. Wu, G.-L. Wang, and W. Cho Chew, "Efficient low-frequency inversion of 3-D buried objects with large contrasts," *IEEE Trans. Geosci. Remote Sens.*, vol. 44, no. 1, pp. 3–9, Jan. 2006.
- [34] X. Ye et al., "Application of subspace-based distorted-born iteration method in imaging biaxial anisotropic scatterer," *IEEE Trans. Comput. Imag.*, vol. 6, pp. 1486–1492, 2020.
- [35] J. Zhuo, L. Ye, F. Han, L. Xiong, and Q. H. Liu, "Multiparametric electromagnetic inversion of 3-D biaxial anisotropic objects embedded in layered uniaxial media using VBIM enhanced by structural consistency constraint," *IEEE Trans. Antennas Propag.*, vol. 68, no. 6, pp. 4774–4785, Jun. 2020.
- [36] M. El-Shenawee, C. Rappaport, and M. Silevitch, "Monte Carlo simulations of electromagnetic wave scattering from random rough surface with 3-D penetrable buried object: Mine detection application using the SDFMM," *J. Opt. Soc. Amer. A, Opt. Image Sci.*, vol. 18, pp. 3077–3084, Dec. 2001.
- [37] C. Rappaport and M. El-Shenawee, "Modelling GPR signal degradation from random rough surfaces," in *Proc. IGARSS, Honolulu, HI, USA*, Jul. 2000, pp. 3108–3110.
- [38] K. A. Michalski and J. R. Mosig, "Multilayered media Green's functions in integral equation formulations," *IEEE Trans. Antennas Propag.*, vol. 45, no. 3, pp. 508–519, Mar. 1997.
- [39] Y. Altuncu and R. Temel, "A buried object approach (BOA) for the scattering of electromagnetic waves from 2D rough surfaces," in *Proc. Int. Conf. Electromagn. Adv. Appl.*, Sep. 2011, pp. 1113–1116.
- [40] B. Guan, J. F. Zhang, X. Y. Zhou, and T. J. Cui, "Electromagnetic scattering from objects above a rough surface using the method of moments with half-space green's function," *IEEE Trans. Geosci. Remote Sens.*, vol. 47, no. 10, pp. 3399–3405, Oct. 2009.
- [41] D. E. Lawrence and K. Sarabandi, "Electromagnetic scattering from a dielectric cylinder buried beneath a slightly rough surface," *IEEE Trans. Antennas Propag.*, vol. 50, no. 10, pp. 1368–1376, Oct. 2002.
- [42] Y. Altuncu, "A numerical method for electromagnetic scattering by 3-D dielectric objects buried under 2-D locally rough surfaces," *IEEE Trans. Antennas Propag.*, vol. 63, no. 8, pp. 3634–3643, Aug. 2015.

- [43] E. Tetik and I. Akduman, "3D imaging of dielectric objects buried under a rough surface by using CSI," *Int. J. Antennas Propag.*, vol. 2015, pp. 1–7, Oct. 2015.
- [44] G. L. Wang, T. Barber, P. Wu, D. Allen, and A. Abubakar, "Fast inversion of triaxial induction data in dipping crossbedded formations," *Geophysics*, vol. 82, no. 2, pp. D31–D45, Mar. 2017.
- [45] J. T. Johnson et al., "Backscattering enhancement of electromagnetic waves from two-dimensional perfectly conducting random rough surfaces: A comparison of Monte Carlo simulations with experimental data," *IEEE Trans. Antennas Propag.*, vol. 44, no. 5, pp. 748–756, May 1996.
- [46] J. Li, J. Zhuo, Y. Chen, F. Han, and Q. H. Liu, "Retrieval of composite model parameters for 3-D microwave imaging of biaxial objects by BCGS-FFT and PSO," *IEEE Trans. Microw. Theory Techn.*, vol. 68, no. 5, pp. 1896–1907, May 2020.
- [47] T. Lan, N. Liu, F. Han, and Q. H. Liu, "Joint petrophysical and structural inversion of electromagnetic and seismic data based on volume integral equation method," *IEEE Trans. Geosci. Remote Sens.*, vol. 57, no. 4, pp. 2075–2086, Apr. 2019.
- [48] F. Han, J. Zhuo, S. Lu, J. Wang, and Q. H. Liu, "Explicit semianalytical expressions of sensitivity matrices for the reconstruction of 1-D planarly layered TI media illuminated by 3-D sources," *IEEE Trans. Antennas Propag.*, vol. 70, no. 2, pp. 1547–1552, Feb. 2022.
- [49] K. A. Michalski, "Extrapolation methods for Sommerfeld integral tails," *IEEE Trans. Antennas Propag.*, vol. 46, no. 10, pp. 1405–1418, Oct. 1998.
- [50] D. E. Livesay and K. Chen, "Electromagnetic fields induced inside arbitrarily shaped biological bodies," *IEEE Trans. Microw. Theory Techn.*, vol. MTT-22, no. 12, pp. 1273–1280, Dec. 1974.
- [51] A. Lakhtakia and W. S. Weiglhofer, "Time-harmonic electromagnetic field in a source region in a uniaxial dielectric-magnetic medium," *Int. J. Appl. Electromagn. Mech.*, vol. 8, no. 2, pp. 167–177, 1997.
- [52] L. Tsang, J. A. Kong, K.-H. Ding, and C. O. Ao, *Scattering of Electromagnetic Waves: Numerical Simulations*. New York, NY, USA: Wiley, 2001, ch. 2.



Ruidong Huang received the B.E. degree in Internet-of-things engineering from Anhui University, Hefei, China, in 2021. He is currently pursuing the master's degree with Xiamen University, Xiamen, China.

His research interests include electromagnetic scattering and inverse scattering in complex media.



Qing Wu received the B.E. degree in electronic information engineering from Anhui Jianzhu University, Hefei, China, in 2019. He is currently pursuing the master's degree with Xiamen University, Xiamen, China.

His research interests include electromagnetic inverse scattering and full-wave inversion.



Feng Han (Senior Member, IEEE) received the B.S. degree in electronic science from Beijing Normal University, Beijing, China, in 2003, the M.S. degree in geophysics from Peking University, Beijing, in 2006, and the Ph.D. degree in electrical engineering from Duke University, Durham, NC, USA, in 2011.

Since July 2015, he has been with Xiamen University, where he is currently an Associate Professor of the Institute of Electromagnetics and Acoustics.

He has published more than 50 articles in refereed journals. His research interests include electromagnetic scattering and inverse scattering in complex media, multiparametric and multidimensional hybrid electromagnetic full-wave inversion, fast electromagnetic full-wave inversion based on machine learning, configuration of the antenna array for electromagnetic inverse problems, and geophysical electromagnetic exploration and inversion.